Design and Application of Imaging Plasma Instruments

C. W. Carlson and J. P. McFadden

Space Sciences Laboratory, University of California, Berkeley

Imaging particle detectors based on the cylindrically symmetric "top hat" analyzer optics are used in plasma instruments for many of the current generation of spacecraft, including Wind, Cluster, Fast, Mars Observer, Mars Global Surveyor, Lunar Prospector, and numerous sounding rockets. These instruments are designed to provide rapid measurements of particle distribution functions with good phase space resolution. Design details can be optimized for measuring specific plasma populations, such a cold beams, hot distributions, or loss cone features. The top hat geometry is a simple extension of traditional spherical section electrostatic analyzer optics, but there are several interacting design parameters that are not uniquely determined. For specified values of geometric factor, energy resolution and angular acceptance, analytic expressions can be used to specify preliminary mechanical dimensions. This initial design is then optimized by a computer trajectory-tracing program that accounts for additional design details such as input aperture collimation and particle detector location, or other optical elements such as input deflectors or time-of-flight detectors. Once the optical design is specified, additional design considerations are addressed, such as the particle detection method, suppression of UV and electron scattering, contamination control, electrical interfacing, and general mechanical packaging. Examples of several current flight instruments are described.

INTRODUCTION

The scientific goals of most contemporary plasma physics missions require rapid, accurate 4π sr measurements of plasma distribution functions. The following examples of measurement objectives relate to several current space missions for which we have designed instruments. The WIND 3-D plasma experiment measures electrons and ions with energies between 3 eV and 30 keV. The spacecraft traverses a wide range of plasma conditions, including the solar wind, and the Earth's bow shock, magnetosheath, and magnetosphere. Measurements in these regions require wide dynamic range and the ability to resolve 3D structure of distributions ranging from intense fluxes of cold, streaming solar wind ions to very tenuous plasmas such as energetic solar electrons. The CLUSTER mission will study plasma properties similar to those of WIND but will emphasize the 3D structure of plasma boundaries. Instruments will encounter the cold solar wind ion beam, warm streaming ion distributions in the magnetosheath, hot tenuous ion distributions in the magnetosphere, and will perform mass resolved measurements in all regions. Instruments must have adequate dynamic range to make accurate measurements while crossing these boundaries and good absolute accuracy to allow inter-comparison of measurements from four spacecraft. The Mars Global Surveyor and Lunar Prospector electron reflectometer experiments will investigate Martian and Lunar surface magnetic structure by accurately measuring the loss cone signature of electrons that mirror near the surface and return to the spacecraft. The FAST mission investigates microphysics of

Measurement Techniques in Space Plasmas: Particles
Geophysical Monograph 102

auroral acceleration. This objective requires very rapid measurements of high contrast electron distributions in inverted Vs and field aligned electron beams as well as the angular distributions and mass composition of precipitating ions, ion conics, and ion beams. The cylindrically symmetric top hat electrostatic analyzer has found wide application in the present generation of plasma instruments owing to a number of attractive properties. It has a uniform 360° field of view with azimuth angle imaging, a nearly Gaussian energy and angle response, a large geometric factor, low mass, and is easily coupled to a variety of detector systems. This paper describes the salient features of several of these instruments and discusses technical issues that were addressed during their design and construction. It is not intended as a comprehensive review of contemporary plasma instruments, but will discuss design considerations common to many of them. The paper first addresses the analyzer optical properties. The second section discusses applications to specific experimental requirements that mainly determine the detection systems that follow the analyzer. The final section presents a description of specific flight instruments and a discussion of some of the technical issues related to building these instruments.

ANALYZER OPTICS

The concept for the 360° angle imaging top hat electrostatic analyzer was introduced by *Carlson et al.* [1983] as a means of extending the angle imaging properties of the quadrispherical plasma analyzer design [*Bame et al.*, 1978; *Frank et al.*, 1978] to a uniform response with 360° field of view. The initial paper was a brief report of general design principles, some computer simulation results, and laboratory measurements of a prototype analyzer. It was first applied to space plasma investigations on sounding rockets [*McFadden et al.*, 1986] and with the 3D plasma instrument on AMPTE IRM [*Paschmann et al.*, 1983]. More extensive discussions of computer simulations of the spherical top hat performance were presented by *Sablik et al.* [1988]. *Young et al.* [1988] presented simulation and prototype test results of a toroidal top hat analyzer geometry which demonstrates longer focal length properties that are better suited for coupling to a mass resolving time of flight detector section.

ANALYTIC DERIVATION

The top hat optics were originally modeled analytically, an approach that is useful for understanding how the various design parameters determine the particle trajectories, and for estimating optimum values of these parameters. The "generic" analyzer design is illustrated in figure 1. The main design parameters, plotted in figure 2, can be derived from elementary principles. The analyzer constant $K=R_1/\Delta$ (where $\Delta=R_2-R_1$) is the principal parameter that determines the geometric factor, energy to voltage ratio, and other properties of the analyzer. If the outer hemisphere is grounded and the inner hemisphere is set to a potential V, one can show that a particle of charge q and external kinetic energy $T_0=-KqV/2$ will follow a circular trajectory that just grazes the outer radius R_2.

The value of the top hat radius R_3 and opening angle θ have interactive effects that determine the effective entrance aperture and the average elevation angle of accepted trajectories. Their values are chosen to obtain maximum geometric factor and an angular field of view that is perpendicular to the analyzer axis. The maximum geometric factor is realized if the top hat entrance aperture is at least as large as the analyzer plate gap Δ, so the minimum top hat radius is approximately $R_3=R_1+2\Delta$. Larger values of R_3 are undesirable since they provide no significant increase to the geometric factor and shift the average elevation angle upward from the axis normal. The selection of the top hat angle θ is adjusted to optimize the alignment of the entrance aperture with trajectories that will pass through the main section of the analyzer. A convenient way to visualize this condition is to run trajectories backward through the analyzer, and see where the top hat aperture must be located for these trajectories to escape. The radius of an escaping trajectory must lie between R_2 and R_3 at the exit, so its radius must increase as it passes through the top hat region. If θ is too small, the radius of many trajectories will not increase sufficiently to escape. If θ is too large, many of the trajectories will hit the top hat before reaching the exit.

The motion of particles through this region can be easily calculated. The electric field between the hemispherical plates is inversely proportional to the gap spacing, and the radius of curvature of the particle also varies inversely with the field, so the radius of curvature of a particle that has a "grazing" trajectory in the main section of the analyzer will traverse the top hat region with a radius of curvature equal to $2R_2$. We want the path of the "grazing" particle to be perpendicular to the analyzer axis, so the center of curvature, C, must be aligned vertically below the top hat entrance, as drawn in fig. 1. The trajectory shown in this diagram has a smaller radius than the grazing trajectory so that its complete path through the analyzer would be visible. The analyzer parameters will be chosen such that this "grazing" particle entering the analyzer would just graze the lip of entrance gap at a radius R_3 before continuing through the top hat region to the main analyzer section, where it enters tangent to the outer plate. We define R_g to be the value of

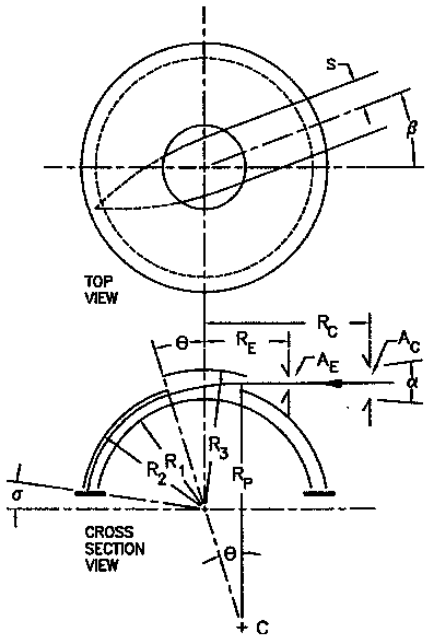

Fig. 1. Top and cross-section views of top hat analyzer identifying principal design parameters. A typical particle trajectory is shown. The particle's radius of curvature through the top hat region is approximately 2 R_2 with a center of curvature at C.

R_p for this grazing trajectory which just touches the lip of the top hat entrance. This point is spaced approximately a distance Δ above the lip of the outer hemisphere. A right triangle can be constructed that connects the center of curvature, *C*, to the two edges of the center hole in the outer hemisphere. From this construction, one can show:

$$2R_2\cos\theta = R_g - \Delta = 2R_2 - \Delta$$

$$\text{so,} \quad \cos\theta = 1 - \frac{\Delta}{2R_2}$$

Since theta and Δ/R_2 are relatively small, we expand both sides of the equation,

$$\cos\theta \sim 1 - \frac{1}{2}\theta^2 + \frac{1}{6}\theta^4$$

and

$$1 - \frac{1}{2}\frac{\Delta}{R_2} \sim 1 - \frac{1}{2}\frac{\Delta}{R_1}\left(\frac{1}{1+\frac{\Delta}{R_1}}\right) \sim 1 - \frac{\Delta}{2R_1}\left(1 - \frac{\Delta}{R_1}\right)$$

so to order Δ/R_1 we have,

$$\theta \sim \sqrt{\frac{\Delta}{R_1}}$$

The values of the top hat gap and theta angle are coupled with the choice of the mean elevation angle of the detector response.

The angle focussing properties of the analyzer results from spherical symmetry. In a spherical section analyzer, particles entering on parallel paths travel great circle trajectories that converge at the analyzer exit. The electric field in the top hat region, however, is not quite spherically symmetric. There are two major competing contributions to the focusing field in the top hat region. The total field strength is reduced because of the increased gap, but the curvature of the field is greater because of the geometry of the boundary conditions. The net result of these competing effects is that the angular focus is shortened from the 90° plane by the truncation angle σ which is ~θ/2. The fringing fields near the periphery of the top hat are quite strong, so trajectories passing through the entrance far from the center line (larger value of "s" in fig. 1) are focussed more strongly and converge before the principal focal point. The resulting image of a parallel particle beam is not a delta function, but a sharply peaked distribution with slight wings on each side of the central focus.

The "flat top" toroidal geometry discussed by *Young et al.* [1988] provides a longer focal distance. The combination of reduced field curvature in the top hat region and the intrinsic astigmatic response of the toroid geometry places the average focus beyond 90°, which is advantageous for coupling to a time-of-flight detector system. The penalty of this longer focal distance is a greater aberration due to fringing fields, resulting in a broader focal plane image. The Codif and Teams detector designs use a modified toroid geometry that extends the focal point beyond 90° but has less image aberration than the flat top toroid [*McFadden and Carlson*, this volume].

The velocity space volume accepted by the analyzer is extrapolated from the value derived for a quadrispherical analyzer [*Gosling et al.*, 1978], which also gives good agreement with experimental results:

$$\left\langle \frac{dv}{v} d\alpha \right\rangle = \frac{1}{4}\left(\frac{\Delta}{R_1}\right)^2 \csc^3\left(\frac{90-\sigma}{2}\right)\left(\frac{7}{8} + \cos\left(\frac{90-\sigma}{2}\right)\right)$$

The accessible entrance area is estimated as 2/3 of the projected aperture area, so:

Aperture area = $\frac{2}{3}\Delta R_1 2\theta$, therefore the resulting "velocity" geometric factor for a 360° field of view is:

$$G(v) = 4\pi \cdot \frac{2}{3}\left\langle \frac{dv}{v} d\alpha \right\rangle \frac{\Delta}{R_1} \cdot \theta \cdot R_1^2$$

The more commonly used "energy" geometric factor is:

$$G(E) = 2G(v)$$

The nominal values for the design parameters vs. Δ/R_1 are shown in fig. 2. These values do not take into account any effects of input collimation, which will decrease the phase space acceptance and geometric factors.

SIMULATIONS AND MEASUREMENTS

The analytic model is useful for estimating the geometric factor and approximate response for an analyzer design, but

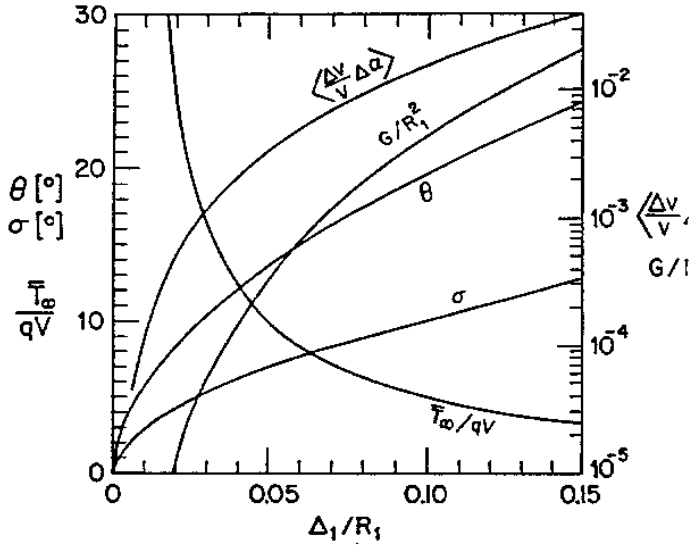

Fig. 2. Summary of analyzer parameter vs. Δ/R_1. These values to optimize angle focussing at the analyzer exit position. The values for G are the "velocity" geometric factor which is one-half the value of the "energy" geometric factor. These curves provide a useful starting point for analyzer designs but computer ray tracing is needed to optimize practical mechanical designs.

it is not accurate enough for working designs. Actual design requirements include collimators and other mechanical features that affect the optics and are not easy to model analytically. Testing the response of an analyzer typically requires a test facility with a well defined ion or electron source and a multi-axis manipulator that can rotate and translate the detector to map out its response. A good computer simulation can evaluate a design much more quickly and easily than laboratory tests. A ray tracing program also gives much more information about the actual trajectories of particles than can be obtained from any practical laboratory calibration. All of the optics described below were designed by computer simulation. The final detector calibration was carried out to verify the agreement with simulations. A detailed description of the simulation procedure is described in a companion paper [*McFadden and Carlson,* this volume].

The simulations presented in the following discussion were made for electron instruments for the FAST satellite. These analyzers have an inner plate radius of 3.75 cm and Δ/R of 0.06. They also have a 8.125 mm wide collimator aperture at a radius of 5.725 cm that serves to reduce UV access to the detector and also reduces the wings of the angle/energy response. The measurements that are shown below are from the calibration of flight instruments. The calibration facility uses an automated three axis manipulator that can vary the elevation angle, rotation angle, and position along the detector axis. The electron source is a photoelectron cathode that supplies a uniform circular parallel beam with a diameter larger than the entrance aperture. The instrument operation, electron gun, and manipulator are all controlled by a computer that automatically collects measurements over the entire angle and energy range of the analyzer. Other tests performed during calibration include measuring the sensitivity of the instrument to UV photons from a hydrogen discharge lamp and absolute cross-calibration using a Ni^{63} beta source.

The computer simulation provides a complete representation of the analyzer energy and α angle response. This response, plotted in fig. 3a, illustrates the expected angle/energy skew that is characteristic of a 90° analyzer. Comparison with measured data is easier to interpret if these data are collapsed onto two separate plots that show the integrated energy and angle responses. The energy response data in fig. 3b were measured at a fixed rotation angle with a gun energy of 10 KV. The multiple overlapping traces at the bottom of the plot are energy scans for 1° increments of α angle. The measured response integrated over α angles is plotted as open circles. The results of the computer simulation are shown as + symbols. The simulation results can be fit very closely by a Gaussian function, plotted as a dashed line. The agreement between simulation and measurement is generally good, although the measured response appears to be about 8% wider than the simulation. When a similar analyzer was calibrated using an ion beam the agreement with the simulation was nearly exact. The difference in behavior between the ion and electron measurements is attributed to the greater probability of small-angle scattering by electrons that results in a less abrupt cut-off in the energy response. The effective energy width is also greater so the geometric factor is also correspondingly larger.

The α angle response shown in fig. 3c is constructed from the same simulation and calibration data as in fig. 3b. In this case, the data are integrated over energy and the plot again shows experimental data and a Gaussian fit to the simulation data. It is fortuitous that the analyzers angle and energy response are so nearly Gaussian, since it is a particularly convenient weighting function for deconvolving the measurements. For example, the effect of the analyzer response on the measurement of a streaming thermal distribution such as the solar wind is to increase the apparent temperature by a small known factor. This calculation is particularly simple since the convolution of two Gaussians is also Gaussian with a width equal to the rms sum of the widths of the original Gaussians.

The energy response curve in fig. 3b can be fitted by a Gaussian using velocity as the variable. The velocity width is simply half of the energy width, and the functional expression for transmission is:

$$N = \exp\left(\frac{(v - v_0)^2}{w^2}\right) \text{ where } w = .045v_0.$$

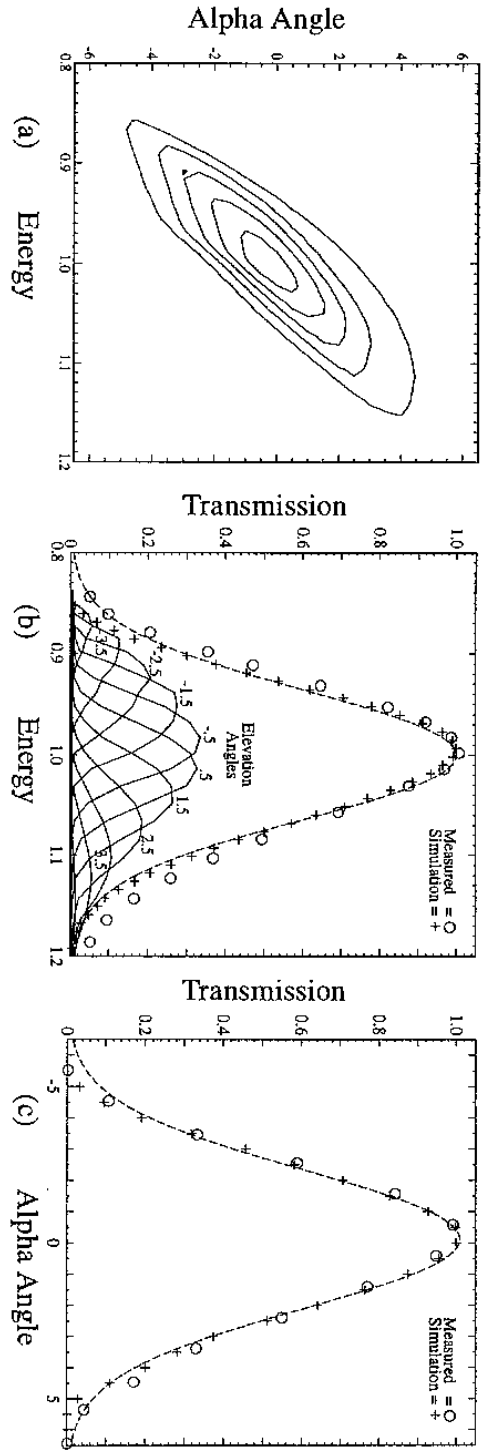

Fig. 3. (a) Input energy-angle response contours obtained by computer particle tracing. Contours are spaced by 20% steps. (b) Energy dependence of analyzer transmission obtained from calibration of a FAST flight instrument. Measurements are shown for the individual contributions from 11 incremental alpha angles as well as the integrated response. Agreement with simulation data is generally good, but the measured response is broadened by electron scattering within the analyzer. Calibration with an ion source demonstrates nearly exact agreement with the simulation. The dashed line represents a Gaussian fit to the simulation data. (c) Elevation angle response integrated over energy. Simulation and measured data show excellent agreement.

If the solar wind is modeled as $f = f_0 \exp\left(\frac{(v - v_0)^2}{v_{th}^2}\right)$ then the measured distribution will have an apparent thermal velocity $v_{meas} = \sqrt{(v_{th}^2 + (0.045 v_0)^2)}$. For a solar wind with a temperature of 10 eV and flow energy of 1 keV the broadening of the measured temperature is only 2 eV, and this deconvolution can be accurately and easily applied. The perpendicular temperature measurement is broadened by a similar amount owing to the convolution with the α angle response. Although these temperature corrections can be applied rather simply, more sophisticated applications using the full momentum flux tensor should also account for the analyzer's energy-angle skew.

Uniform sampling of phase space is an important requirement for many plasma measurements. On a spinning spacecraft, the 360° top hat analyzer can sample 4π sr in one half spin period. To achieve uniform sampling, the energy sweep period must be shorter than the time for the spacecraft to rotate through the angular width of the analyzer field of view. The full $1/e$ Gaussian width (fig. 4) for the WIND PESA-L analyzer is slightly greater than 6°. A sweep frequency of 64 sweeps/spin produces an angular separation between sweeps of 5.625°, which is an ideal match to the analyzer width. The sweep overlap and resulting superposition response is plotted in fig. 4. This plot is the response for a parallel beam. Even a beam as narrow as the solar wind will allow the response to be almost flat. For a Gaussian angular response function, the composite response is uniform to a few percent for any sweep spacing smaller than 90% of the full $1/e$ response width. An alternative method of meeting the sample requirement with a

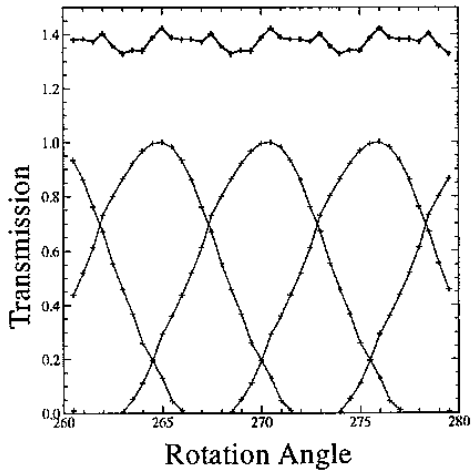

Fig. 4. Composite response for a rotating, energy sweeping analyzer. The lower set of curves are the instantaneous angle response at each 5.5° angle of rotation. The top curve is the resulting response obtained by combining the individual energy sweeps.

lower sweep frequency is to use a full spin period for the measurement with 31 or 33 sweeps per spin. The angular slices on the two half spins are interleaved for any odd number of sweeps.

Another factor related to uniform detector response is the location of posts supporting the collimation apertures, top hat and any analyzer cover. These posts can modulate the angular response if they are located incorrectly, especially if they block much area. The criteria for post location can be found by considering the inverse response, which is the analyzer response to an aperture composed of equally spaced thin slits. In order that the azimuthal response be uniform, the separation distance between the slits must be equal to the effective aperture width. Since the transmission of the top hat drops rapidly for trajectories that have a separation from the centerline greater than about 0.6 of the top hat radius (see fig. 1), the optimum angular spacing of the slits depends on the collimator aperture radius R_c. The final combination of radius and slit spacing can be found by trial and error using simulations. The Mars Observer analyzer had rather wide aperture posts that were part of a variable input attenuation system. Figure 5 demonstrates the slit response data that were used to choose the location of posts for that instrument. Although the slit response has variations of 10% or so, the posts will introduce very little modulation to the response, since their total attenuation is typically only about 5%. In order that posts give uniform attenuation, they should be located at the same angular separation as calculated for the optimized slits.

The focal plane angular response of the spherical top hat analyzer can be very narrow when the optimum truncation

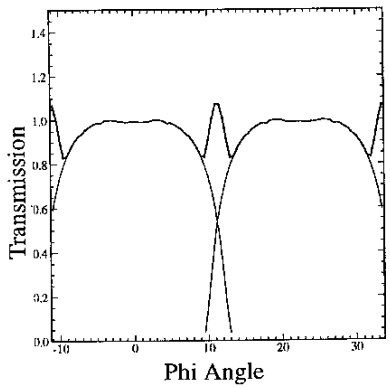

Fig. 5. The Beta (azimuthal) angle response of a narrow vertical entrance slit collimator to a parallel particle beam. The response shows a simulations of the Mars Observer analyzer for a slit separation of 22.5° (16 equally spaced slits). The radial location of the slits has been selected for minimum modulation of the composite response.

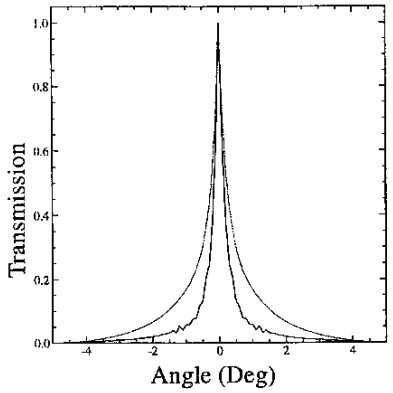

Fig. 6. The azimuth (beta) angle focussing for the FAST analyzers. The solid line is the differential response. The shaded line is the integral response representing the fraction of particles lying outside of the corresponding angle. The angular focussing depends upon value of the truncation angle sigma. Susceptibility to UV background becomes worse with larger values of sigma. This FAST design accepted slightly degraded focussing to improve UV rejection.

angle σ is used. Fig. 6 shows results of a simulation that convolves the analyzer response over energy and elevation angle for a beam with a fixed azimuth angle. The two curves show the normalized beam image (solid line) with 0.1° bin resolution, and the integral beam response, integrated inward from 5° toward smaller β angle (dashed line). The integrated beam represents the fraction of trajectories that lie outside the angular width β, which is a better representation of optimal focussing. The $1/e$ full width is narrower than one degree, and 90% of the particles fall within 3° full width. This resolution is more than adequate for practical resolution of solar wind or auroral beams. Narrow depletions in the angular distribution are more difficult to resolve because of the wings at the few percent response level. The toroidal focus response will have a wider spread than this plot because the variation in focal length with changing input position is greater for the toroid. Since the toroid analyzer can have an arbitrary value of major and minor radii, it is difficult to show a "typical" response for toroidal analyzers.

Deflection plates are a useful accessory that can steer the field of view of an analyzer. This ability is essential on a non-spinning spacecraft, and provides other flexibility, such as tracking particle beams or the magnetic field vector. Fig. 7 illustrates the deflection system which was included on the high sensitivity electron analyzer EESAH of the Wind 3D plasma instrument [*Lin et al.*, 1995]. Only positive deflection voltages are used, to avoid producing beams of energetic photoelectrons that might contaminate other mea-

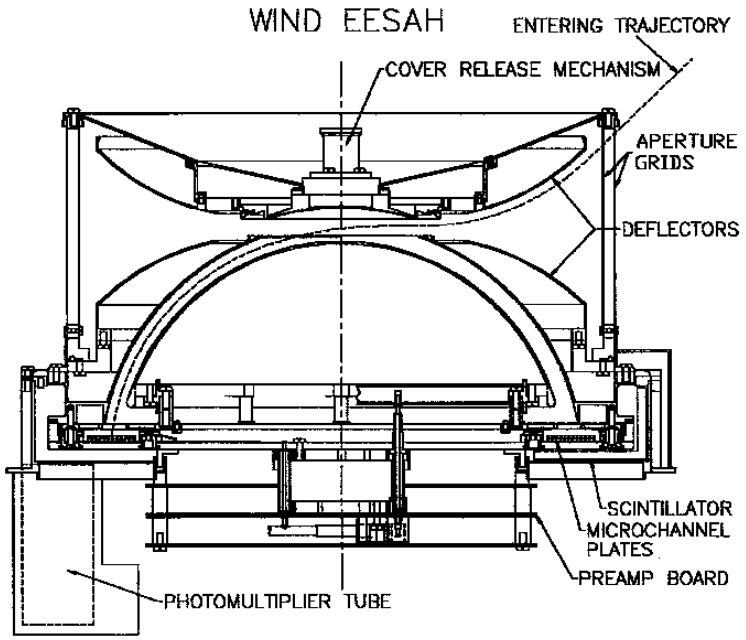

Fig. 7. The large electron analyzer, EESA-H, for the Wind 3-D Plasma Instrument. Deflection plates are used to deflect the analyzer field of view by +/- 45°. This figure also illustrates the anti-coincidence scintillator used to reject penetrating particle background counts.

surements. In operation, one plate is driven to a positive potential while the other is held at ground. The entrance aperture is covered by a double grid system that eliminates any significant leakage field. The analyzer geometric factor and energy response are nearly constant for any deflection angle between ± 45°. The deflection angle versus the ratio of deflector to analyzer voltage is shown in fig. 8.

One of the penalties of a large aperture, short deflection angle analyzer is its susceptibility to UV photon contamination. A number of measures are taken to reduce the amount of UV that can be transmitted to the detection system following the analyzer. Multiple baffle collimators (see fig. 9) at the entrance reduce the access for UV to the minimum solid angle that is required for admitting the desired charged particles. A photon must scatter a minimum of two times before reaching the analyzer exit. All surfaces that are critical for UV scattering are scalloped and blackened with vacuum deposited "gold black". Scalloping of the top hat and outer hemisphere surfaces (fig. 9) eliminates small angle specular reflection of photons except at the sharp cusp between each scallop. The effectiveness of scalloping is seen in fig. 10. This figure shows the α angle dependence of UV rejection and the relative effectiveness of scalloping the outer hemisphere and top hat. There is a minimum at zero degrees elevation where photons pass straight through the aperture. For negative angles, the minimum path for a photon includes one scatter off the inner top hat surface and one scatter on the outer hemisphere surface. Scalloping reduces

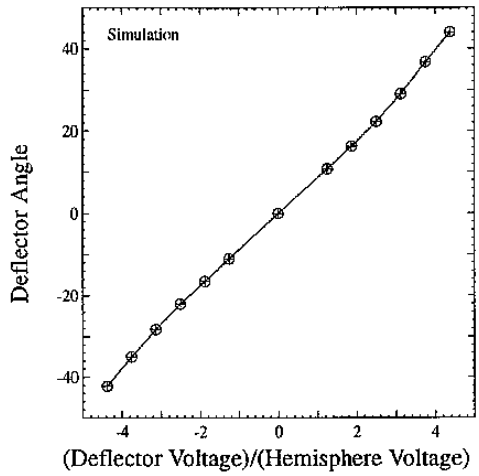

Fig. 8. The dependence of deflection angle on the deflector voltage. The deflection voltage is normalized to the analyzer hemisphere voltage. The deflection angle response is nearly linearly dependent on the voltage ratio over the full deflection angle range. The analyzer transmission properties are also nearly constant over this range.

the scattering efficiency by a factor of three on each surface, or a factor of 10 overall. Photons entering at positive angles suffer two successive scatters on the outer hemisphere surface, so the top hat scalloping has no significant effect.

A second test was run to measure the contamination of low energy electron measurements by UV. The data shown in fig. 11 were obtained in the normal operating conditions with an accelerating voltage of +500 volts on the front of the MCP. In this configuration, photoelectrons created with the appropriate velocity within the electrostatic analyzer can travel to the MCP and be counted. Most of the photo-

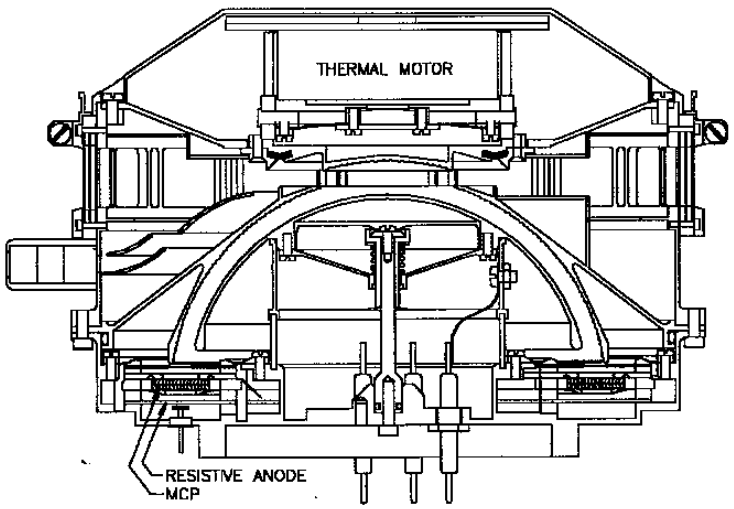

Fig. 9. The Mars Observer Analyzer. This figure illustrates the scalloping of the analyzer surfaces that improves UV rejection. This design used resistive anode image decoding. Other specialized features include a reclosable top hat seal, input attenuator grids, and separate low energy retarding potential analyzer entrance (the small tube projecting from the left side of analyzer).

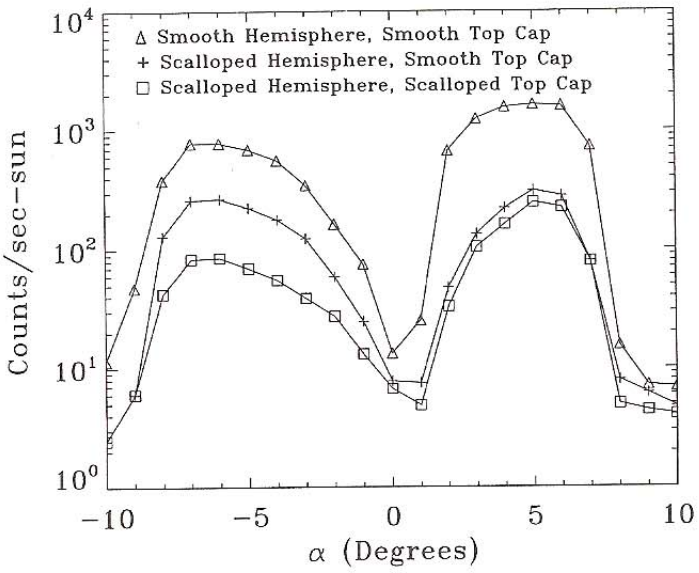

Fig. 10. UV response for three different analyzer surface configurations. The intensity is normalized to the solar Lyman alpha intensity. All tests used "gold blackened" surfaces. The response for smooth surfaces is slightly more than 10^3 counts/sec-sun at the most vulnerable angle. The path through the analyzer requires a minimum of two scatters off the hemisphere or top hat surfaces. The data show that scalloping improves the attenuation by about x3 for each scatter.

electrons are relatively low energy, so the level of contamination is very sensitive to the analyzer plate voltage. The background count rate due to photoelectrons at 1 eV is three decades higher than at 10 eV. At 30 eV the rate has decreased to less than 100 counts/sec for a unit solar intensity input. This contamination is a severe problem for experiments attempting to measure very low energy solar wind electrons. *Alsop et al.* [this volume] identify this potential problem for the PEACE experiment on the Cluster mission and have developed a baffle at the entrance of the analyzer that is designed to absorb photons at their first impact.

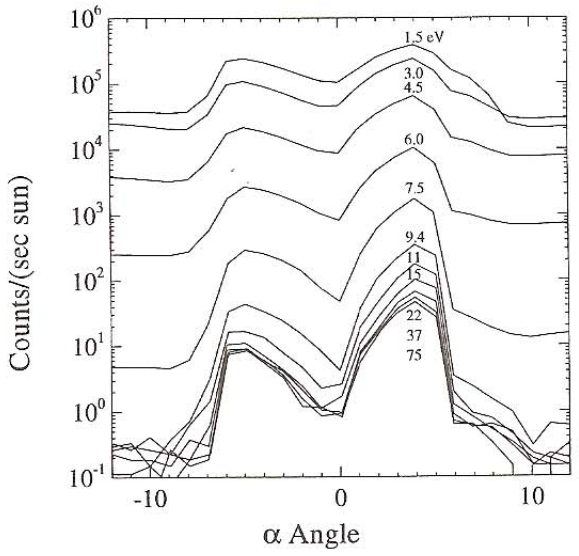

Fig. 11. UV response for producing photoelectrons with the analyzer. Curves are labelled for values of analyzer pass energy between 1.5 and 75 eV. The response for energy settings higher than 10 eV is mainly due to scattered photons reaching MCP (compare with fig. 12). The amount of background from photoelectrons increases rapidly for energies below 10 eV.

DETECTION METHODS

The electrostatic analyzer selects plasma particles that meet specific energy and angle criteria and images their exit position according to their incident angle. Some form of position sensitive detector is typically placed at the analyzer exit to register the particles arrival. The following discussion addresses various methods of position sensing detection. More complex detection systems such as time-of-flight mass discrmination [see *Moebius et al.*, this volume] are beyond the scope of this discussion. This review of detection methods will lead to a discussion of specific design examples, which includes their scientific requirements as well as the technical approaches.

Three position resolving detection methods that we have used for flight detectors are represented in fig. 12. All three approaches use an electron multiplier to convert and amplify the initial charged particle impact to an electron pulse that can be amplified and discriminated electronically. The first method, using an array of channel electron multipliers, was used for the AMPTE IRM 3D plasma instrument [*Paschmann et al.*, 1983] and the Freja TESP detector [*Boehm et al.*, 1994]. This approach uses the oldest technology of the examples presented here. It works reliably but has a number of disadvantages relative to the MCP (microchannel plate) systems. Some of the specific limitations for this detector type are the following: Channel multipliers typically have entrance apertures that cannot be mounted contiguously so there is significant dead area between each channel; Channel multipliers have high gain, ~10^8 electrons/event, so they require significant power if designed for high count rates; multiple channel multipliers are bulky and expensive relative to MCPs. Because of these limitations the channel multipliers has been replaced by MCPs in most recent imaging applications, but is included here for historical reference.

Detectors based on MCP multipliers are the most prevalent type of imaging detectors. These include: discrete anodes; charge division decoding such as resistive anodes and wedge & strip anodes; delay line anodes; and hybrid systems that use interleaved electrodes and coincidence logic [*Johnstone et al.*, 1993]. A variety of imaging meth-

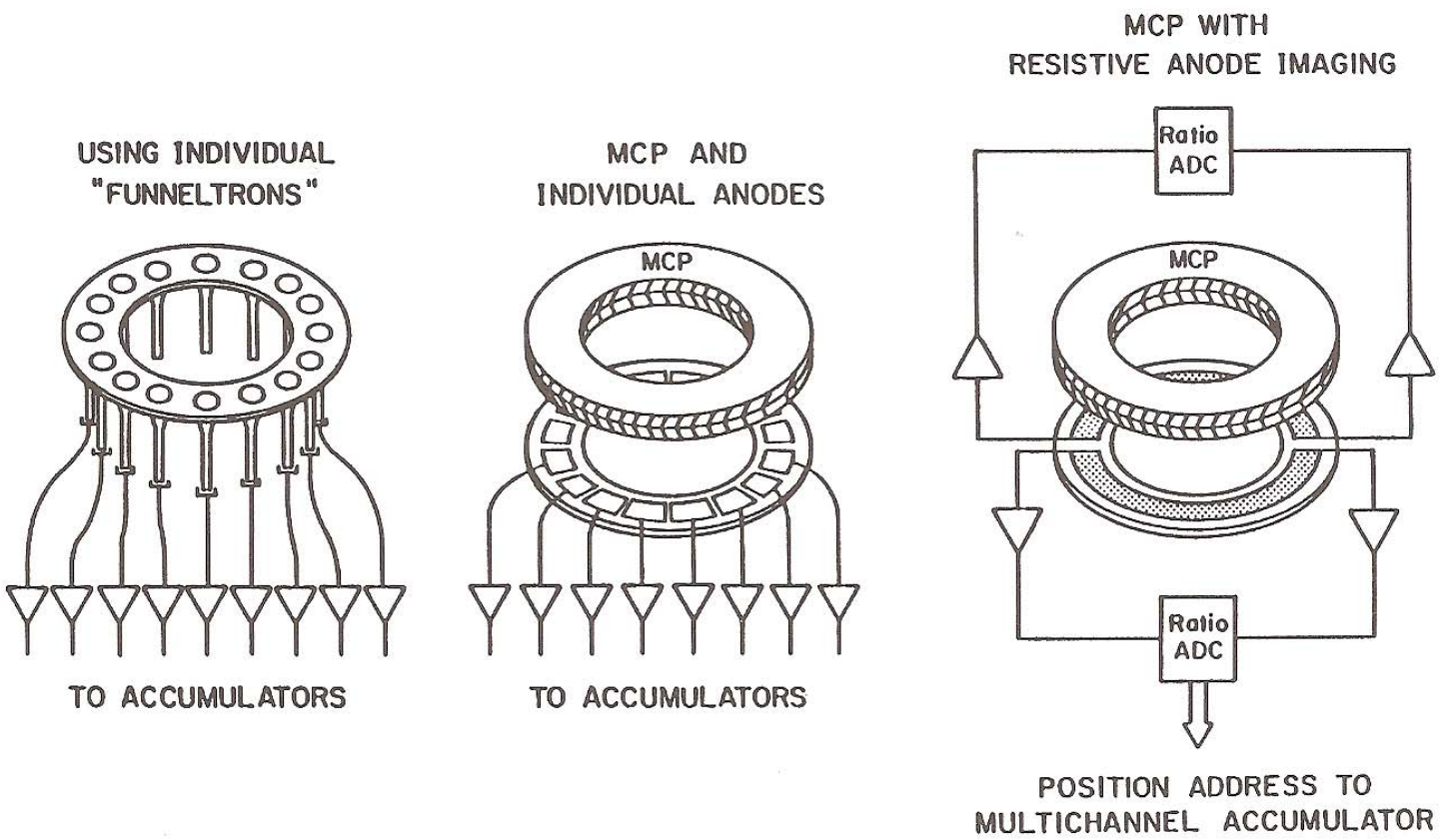

Fig. 12. Three of the more commonly used detector systems used with electrostatic analyzers are individual channel electron multipliers, MCPs with discrete anodes, and MCPs with image decoding.

ods, including those mentioned above, are discussed in a recent summary prepared by *Siegmund et al.* [1992]. The two methods illustrated in fig. 12 are the discrete anode and resistive anode systems, which are used in the detector systems considered here.

There are many detector applications that can be satisfied equally well by either discrete anodes or image decoding systems. Systems with a large number of image channels (pixels) strongly favor image decoding systems, whereas high speed and simplicity are the defining characteristics of discrete anode systems. These two methods also have quite different requirements for MCP performance.

Speed is an important factor that favors discrete anodes over image decoding methods. Virtually all image decoding methods have a maximum total event rate that is determined by the decoding electronics system. A typical limit is about 1 MHz for current technology. This rate applies to the combined total of all resolution channels. The complexity of electronics for a discrete anode system scales with the number of pixels, whereas most image decoding systems have a relatively fixed overhead of power, weight, volume, and cost that does not scale with pixel count. The crossover point where imaging has a clear advantage for these resources is typically between 20 and 40 channels. For sheer speed there is no contest. Commercial space qualified MCP pulse amplifiers that are used for the FAST instruments can operate at count rates of 5 MHz with a power consumption of only 25 mW. Our Mars Observer instrument required a 256 channel imaging system, which consumed about 1 watt and had a dead-time limited rate of about 1 MHz. A system of 40 discrete channels would consume the same power and have a rate capacity of 200 MHz.

Applications requiring high resolution, two dimensional imaging, or a large number of pixels obviously favor the image decoding approach. Spacial resolution better than 50 microns and image formats of 1000 x 1000 pixels are achieved with existing systems in astronomy instruments [*Siegmund et al.*, 1992]. An example of a plasma application with somewhat less demanding requirements is the TIMAS instrument for the POLAR mission, which will measure 3-D mass resolved ion distributions [*Walton et al.*, this volume; *Shelley et al.*, 1995]. Hybrid approaches can retain the speed of discrete anodes, and allow increased resolution when lower count rates allow it. One hybrid system, used by the Cluster PEACE instrument [*Johnstone et al.*, 1993], employs a variation of charge division imaging based on discrete anodes that are comb shaped rather than solid electrodes. A second set of electrodes is interleaved between the fingers of the sector anodes, to provide finer resolution. The anodes are spaced sufficiently far from the MCP to allow charge cloud to spread and impinge on both sets of electrodes. The fine imaging is common to all sec-

tors, so coincident logic that combines the fine image with the sector anodes allows high resolution measurements within a selected sector. At high count rates the high resolution decoding will fail, but the coarse discrete imaging is retained.

The two extremes of speed and resolution set similarly diverging requirements for MCP performance. High resolution image decoding requires a good signal to noise ratio and tolerates a relatively limited dynamic range for total pulse amplitude. The resulting MCP requirement is a high saturated gain and narrow pulse height distribution, and count rates per area that are well below levels where MCP gain begins to droop. High resolution systems typically use three plates in a "Z" stack configuration that generates electron gains in the 10^7 range. These large gains reflect the increased number of microchannels that are activated in each successive plate; a single channel in the front plate will excite three or four in the second plate, which then illuminate ten or more channels in the final plate. These final channels typically operate in the space charge limited "saturated gain" regime. Once fired, the microchannel requires time for the plate bias current to replace the charge that was extracted. This time constant can be estimated from the magnitude of the charge pulse and the value of the bias current per channel. Typical recovery times for medium resistance plates run between 50 ms and 1 sec. The effect of this recovery time is complicated to estimate when a large cluster of output channels are triggered by each event because each input channel shares output channels with its neighbors. The net result of high rates is a decrease in gain and broadening of the pulse height distribution. The MCP gain will droop noticeably when the signal current exceeds ~10% of the bias current. Typical image decoding systems cannot tolerate much gain variation before image resolution and detection efficiency deteriorates. Moderate resolution imaging requirements ranging from 100 to 200 channels tolerate lower MCP gains of a few million electrons that can be achieved with a 2 plate "V" configuration.

The limit to the combination of high gain and short recovery time is determined by the MCP strip current or, equivalently, the plate resistivity. The magnitude of the strip current is limited by the thermal dissipation of the plates. The plates have a negative thermal coefficient of resistance, so high current designs must be considered carefully to prevent thermal runaway. The annular geometry of the MCP used for the plasma analyzers mitigates the thermal problem as it has a large perimeter to area ratio and a short, effectively one-dimensional, thermal diffusion path to the edge mounting clamp. Continuous edge clamping is used with all of our designs. The FAST detectors use the highest strip current of the designs presented here, which is 5 uA/cm^2 at a voltage of 1000 volts/plate.

The MCP gain criteria for discrete anode applications are nearly the opposite to those for image decoding. The discrete anodes typically have much less capacitance than wedge and strip or resistive anodes, so the anode/preamp system noise is inherently much lower than for imaging systems. Furthermore, the acceptable signal to noise ratio can be much lower than for imaging, since the only information needed is that the signal safely exceeds the noise threshold. As with imaging systems, the noise level should be made as low as possible and external electrical noise should be minimized. In a well designed system the amplifier threshold can be 2 to 3×10^5 electrons. Consequently, MCP gains in the range of 1 to 2×10^6 provide a comfortable margin for pulse height spread and gain sag. Excess gain margin should be avoided to maximize count rate capability. The discrete anode systems can tolerate greater levels of gain degradation than image decoders. If the pulse height distribution is reasonably sharp, very few counts are lost until the mean pulse amplitude drops to a few times the threshold value.

The characteristics of the electrostatic analyzer operation can allow the MCP to operate successfully at unexpectedly high count rate for certain types of plasma distributions. A cold beam such as the solar wind is one example of such serendipitous conditions. The operation of the 3D plasma instrument on the Wind spacecraft illustrates this example. To achieve overlap in angle coverage, the Wind analyzer makes 64 energy sweeps during the 3 second spacecraft spin. The resulting detector signal is a succession of brief intense bursts of counts that last a fraction of each sweep period. The peak counting rate can be many times larger than the average rate. The beam is cold, so the particles are imaged on a small area of the MCP. In this case, the MCP counting rate limit can be estimated by considering the number of channels available in the area of the image, and the recovery time per channel. The ideal situation is to have a large number of available channels and a recovery time that is less than the sweep period. This analysis also demonstrates why the preferred MCP configuration for high rate applications is a pair of plates in tight contact, so that each event will excite no more than 3 or 4 channels in the rear plate.

The MCPs in the Wind PESA analyzers have about 5×10^3 channels/mm^2. Assuming a solar wind angular scale size of 10°, the corresponding image area on the MCP is 27 mm^2 and contains 1.4×10^5 microchannels. Now consider what transpires when the analyzer sweeps across the beam. Initially each impacting ion triggers a virgin channel, which

excites 3 channels in the rear plate. When 10 percent of the input channels have been triggered, there is a 10 percent chance that an ion will enter a "triggered" channel and not be counted, and approximately a 30 percent chance that the pulse gain will be reduced because a rear channel is depleted. If we arbitrarily choose 10% as a maximum acceptable dead time, approximately 10^4 ions can be detected within each MCP "recovery" time. MCPs can operate with output signal currents equal to about 15% of their bias current with a gain degradation of less than 50% [*Siegmund and Stock*, 1991]. By this criteria, the channel recovery time for the Wind MCPs is approximately equal to the sweep period, so effectively all channels are available for use on each successive energy sweep.

DESIGN EXAMPLES

Numerous plasma instruments have been built during the past decade that use the general optics and detector approaches discussed in the previous sections. In this section, specific designs will be discussed and evaluated. These examples will show the evolution of design improvements, as well as a few approaches that are best forgotten. There are several goals that are common to all the designs, such as: simplicity, accurate and reproducible performance, ease of assembly and repair, contamination control, modularity, integrated radiation shielding, and minimum weight, power, and volume. There are other requirements that are specific to individual designs, such as anti-coincidence systems or deflectors. The following examples illustrate various approaches to meeting these requirements.

MARS OBSERVER, GLOBAL SURVEYOR, LUNAR PROSPECTOR

The electron reflectometer instrument for Mars Observer was designed to measure the small scale magnetic structure near the Martian surface at altitudes below the spacecraft orbit. The electron reflectometry technique uses the information carried by the loss cone signature of reflected electrons to remote sense magnetic field structure [*Acuna et al.*, 1992]. This method requires identifying the loss cone features to an accuracy of a few degrees. The Mars Observer instrument design (fig. 9) uses a resistive anode imaging system to achieve 360° angular measurements with ~ 2° resolution. Contamination control is one of the primary design requirements for MCP systems. The interior volume surrounding the MCPs contains only metal or ceramic components, and is sealed except for the top hat opening. The geometry of the top hat provides a very convenient means for sealing the analyzer until it is in orbit. The entire top hat assembly can be lowered to seal the opening, as shown in fig. 9. An electrically conductive plastic gasket provides a compliant seal against the ring on the outer hemisphere. A cover seal is a standard feature of most of our designs, but for this mission there was a particular concern, because the detector would be in the exhaust plume during several midcourse rocket burns. A re-closable aperture seal was developed, which is actuated by a thermal motor located above the top hat.

The Mars Observer analyzer design includes three separate entrance apertures that are designed to extend its dynamic range for measuring low energy electrons. The main aperture is covered by a high transmission triple grid. The outer two grids are held at ground potential and the potential on the middle grid can be driven negative to stop transmission through the main aperture for low energy electrons. The aperture mounting posts contain slit apertures that allow entry of electrons with an effective aperture area that is 2 percent of the main aperture. When the attenuator is active, the center grid is driven to a negative voltage equal to twice the acceptance energy of the analyzer. The intent is to repel any external electrons that would be accepted by the analyzer. Photoelectrons produced on the grid would also be rejected because they would have an energy double that selected by the analyzer.

The third aperture includes a retarding potential analyzer (RPA) designed to measure thermal electrons. The entrance for this electron path is at the end of the tube extending from the left side of the analyzer (fig. 9). A cylindrical retarding potential lens is housed within this tube, which selects the cutoff energy for entering electrons. The voltage range for this lens is from -10 to +20 volts. When this thermal energy mode is selected, the main aperture grid as well as the post apertures are biased to -25 volts to reject thermal electrons. At the same time, the entire interior structure of the analyzer is biased to +50 volts relative to the retarding voltage. Electrons that enter through the retarding potential aperture are accelerated to 50 eV and are steered through a series of deflection plates and ultimately enter the analyzer aperture. The inner hemisphere voltage is set to accept the electrons from the RPA, which at this point have an energy of 50 eV relative to the analyzer structure. This design is far more complicated than making the measurements with two independent instruments, but resources for additional sensors were not available. This design is the predecessor of the ion RPA for the Cluster CODIF instrument described by McCarthy and McFadden [this volume].

The Mars Observer instrument died with the spacecraft before the start of its primary mission. The instrument did

obtain cruise data that allowed a test of many of its functions. These test revealed the attenuator design was inadequate because a small fraction of the photoelectrons produced on the center grid were able to pass through the analyzer after a single scatter, and produced unacceptable background. Raising the grid voltage to at least five times the acceptance energy would greatly reduce the background by raising the photoelectron energy and thereby causing them to follow a minimum two bounce path through the analyzer.

There will be a new opportunity to accomplish the science objectives with the Mars Global Surveyor mission, and similar objectives of mapping the Lunar Surface will be carried out with a similar instrument on the Lunar Prospector mission. These instruments have been simplified by eliminating the RPA function from the design and replacing the attenuator grids and slits with a separate aperture and deflector system that produces a uniform 2% attenuation that is free of photoelectron problems.

The basic design of the Mars instrument made it difficult to assemble and repair. The MCPs are buried deep within the instrument, so testing and servicing them is inconvenient and risky. This experience motivated the use of more modular designs for recent instruments.

WIND 3-D PLASMA INSTRUMENTS

The Wind 3-D plasma instrument included two pairs of plasma analyzers, EESA-L and -H for electrons and PESA-L and PESA-H for ions, that had widely differing geometric factors and covered the energy range from 3 eV to 30 KeV. They are mounted on short booms to minimize spacecraft potential perturbations for low energy particles and to provide a clear field of view.

The EESA-H analyzer (fig. 7) is very large, with an inner hemisphere radius of 8 cm and Δ/R of 0.075. The geometric factor, after allowing for MCP and grid efficiencies, is 0.1 cm^2-sr-eV/eV. This analyzer provides very high sensitivity measurements of solar wind electrons, such as in type III bursts or the tail of the halo electron distribution. The deflector system allows the analyzer to track the magnetic field through 90° of spacecraft spin to allow a longer measurement of the "parallel" distribution function that should be associated with local production of Langmuir waves. The design also includes an anti-coincidence scintillator that surrounds the MCP assembly and rejects penetrating background events. This background rejection has proved essential for allowing long time averages of high energy electron spectra.

The Wind analyzers include a number of design simplifications and improvements that were motivated by our assembly and testing of the Mars Observer instrument. One of the primary lessons learned was to make the instrument design more modular and serviceable. The analyzer is a complete subassembly that includes the inner and outer hemispheres mounted to a baseplate, an outer housing with apertures, and the top cover with top hat supports. The analyzer can be calibrated as a subassembly and need never be disassembled. Likewise, the MCP anode assembly comprises a multilayer polyimide printed circuit board that includes the metal contacts for the MCP mounting surface, recessed anode electrodes, high voltage and signal traces, and threaded mounting holes for the MCP clamping hardware. Bias resistors, high voltage coupling capacitors, and connector pins are mounted on the surface opposite the MCPs. The polyimide material can be cleaned and baked at elevated temperatures, and has proved compatible with MCP contamination requirements. This anode plate can be completely pre-assembled and tested with MCPs installed. Spare MCPs can be permanently mounted on spare anode boards which are tested, calibrated, and stored as an assembly. A pre-tested anode assembly can be quickly swapped without requiring a major recalibration. The anode boards mount to the base of the analyzer assembly with a few screws, and an O-ring joint seals the interface and provides a compliant mounting. The sweep HV connection for the inner hemisphere is also an integral part of the anode board.

Several measures are adopted to protect the MCPs against contamination. The interior volume of the analyzer that houses the MCPs is isolated from electronic circuitry and other outgassing materials, and is sealed by the top hat cover mechanism until the instrument is on orbit. This cover is designed to vent at a moderate overpressure, which avoids any undue stress on the analyzer or anode plate during testing or as the rocket ascends. The analyzer assembly also has a built-in purge manifold with flow regulator and filter that allows for nitrogen purge during storage and testing. There has been no significant degradation of the MCP performance during the 2 1/2 years since WIND was launched.

The amplifier board is mounted directly to the anode board through a custom-made connector block that includes HV as well as low level signals. The amplifier-discriminators are AMPTEK A-111 hybrid circuits. These circuits are mounted on both sides of the single amplifier board, which is sandwiched between a pair of shield boards. This design provides a compact assembly with very good ground and signal connections between the anode and amplifiers, and

also makes use of the analyzer and anode material as a passive radiation shield.

FAST PLASMA INSTRUMENTS

The FAST (Fast Auroral Snapshot) mission will investigate the microphysics of auroral acceleration processes at altitudes between 350 and 4200 km along an 83° inclination orbit. This objective requires very rapid measurements of electron and ion distribution functions over the energy range from ~3eV to 30 keV. Except for thermal ions, the flow velocities perpendicular to **B** are small relative to the total electron or ion velocities, so 2 dimensional pitch-angle measurements are adequate for most purposes. The spacecraft spin axis will be slightly inclined to the orbit normal, such that the earth's magnetic field will lie within ± 6° of the spin during nearly all auroral crossings. Thus the time resolution for plasma pitch angle measurements is independent of the spacecraft spin period if the detector field of view spans the entire spin plane. FAST includes 16 plasma analyzers with 180° fields of view in the spin plane that can measure pitch angle distributions as often as every 1.6ms. To complement this measurement, the TEAMS instrument (*Moebius*, this volume) has its 360° field of view aligned to include the spin axis so it can measure the full 3-D ion distribution twice during each 5 second spin period.

The FAST analyzers are mechanically and electrically very similar, but are specialized to perform one of three specific functions. All analyzers protrude through the spacecraft skin and have an unobstructed 180° field of view. They function as matched pairs, mounted on opposite sides of the spacecraft, to create a combined 360° field of view. Two of these pairs serve as electron (EESA) and ion (IESA) spectrometers, that sample 48 energies in 32 angle sectors every 78 ms. They provide good energy and angle resolution with a moderate time resolution. These spectrometers have deflection plates that allow the instruments to continuously track the magnetic field direction up to ±10° from the spin plane. The remaining six analyzer pairs are energy stepping analyzers (SESA) that operate as spectrograph channels. In their fastest mode, each pair can measure 16 angle sectors at a fixed energy every 1.6 ms. The time and energy resolution can be traded in binary steps. A 12 point energy distribution can be obtained each 3.3 ms, 24 energy distributions take 6.5 ms and the full 48 energy range requires 13 ms. The energy can be selected from a set of 48 possible levels in binary multiples. For example, the six energies in the fastest mode can be spaced by 1, 2, 4, or 8 of the basic 48 levels. Instrument software can identify interesting regions of the spectrometer energy spectrum for detailed measurement by the spectrograph. This capability will be used by the wave-particle correlator instrument to study wave growth at energies where the electron distribution function has positive slope.

The design philosophy for the FAST instruments was influenced by the large number of analyzers and the weight, size, and cost constraints inherent in the Small Explorer Missions. Manufacturability and ease of assembly were made priority engineering tasks. Plans for refurbishment of MCPs after thermal-vacuum testing mandated easy replacement of pre-qualified MCP/anode modules.

The 16 analyzers are grouped into 4 instrument stacks that are equally spaced around the periphery of the spacecraft instrument deck. One pair contains an electron spectrometer (EESA) and three SESAs and the second pair has the ion spectrometer (IESA) and three SESAs.

The exploded view of the instrument stack (fig. 13) illustrates the major modules that plug together to make up one of the units. The main elements of the analyzer module are two analyzer sub-units that are joined head to head on a common center plate. A counter/preamplifier board is attached to each analyzer pair and electrically mates with the MCP/anode modules. The two analyzer pairs with their preamp boards are mechanically joined and plug to the main interface board, which serves as the command and data interface to the central Instrument Data Processor. The interface board also contains the sweep waveform generator and High Voltage optocoupler circuits as well as the control for the fixed HV supplies and other miscellaneous circuits. The 6 high voltage converters are individual modules that connect to a single HV mother board which, in turn, connects to the main interface. The low voltage converter is mounted to the rear EMC shield, and connects to the main interface via a short cable harness.

The analyzer module contains four analyzers with their MCP anode assemblies attached. The analyzer mechanical components are mostly identical except for a larger radius of the IESA outer hemisphere. Interior details are shown in greater detail in fig. 14. The inner hemisphere mounts to a plastic insulator ring, which is attached to an exit aperture plate. The concentricity and vertical position of the inner hemisphere must be very accurate and stable because the geometric factor varies approximately as the cube of (Δ/R). The plastic ring has small relief slots that allow for the differential expansion between it and the aluminum mating surfaces. The aperture plate attaches directly to the outer hemisphere, which completes the critical alignment path. The outer hemisphere has an external mounting flange that interfaces to the two external shells. Referring to the bottom analyzer in fig. 13, the upper cylindrical shell contains the entrance collimation aperture and connects to the top cover plate. The top hat capsule mounts to the upper shell via a

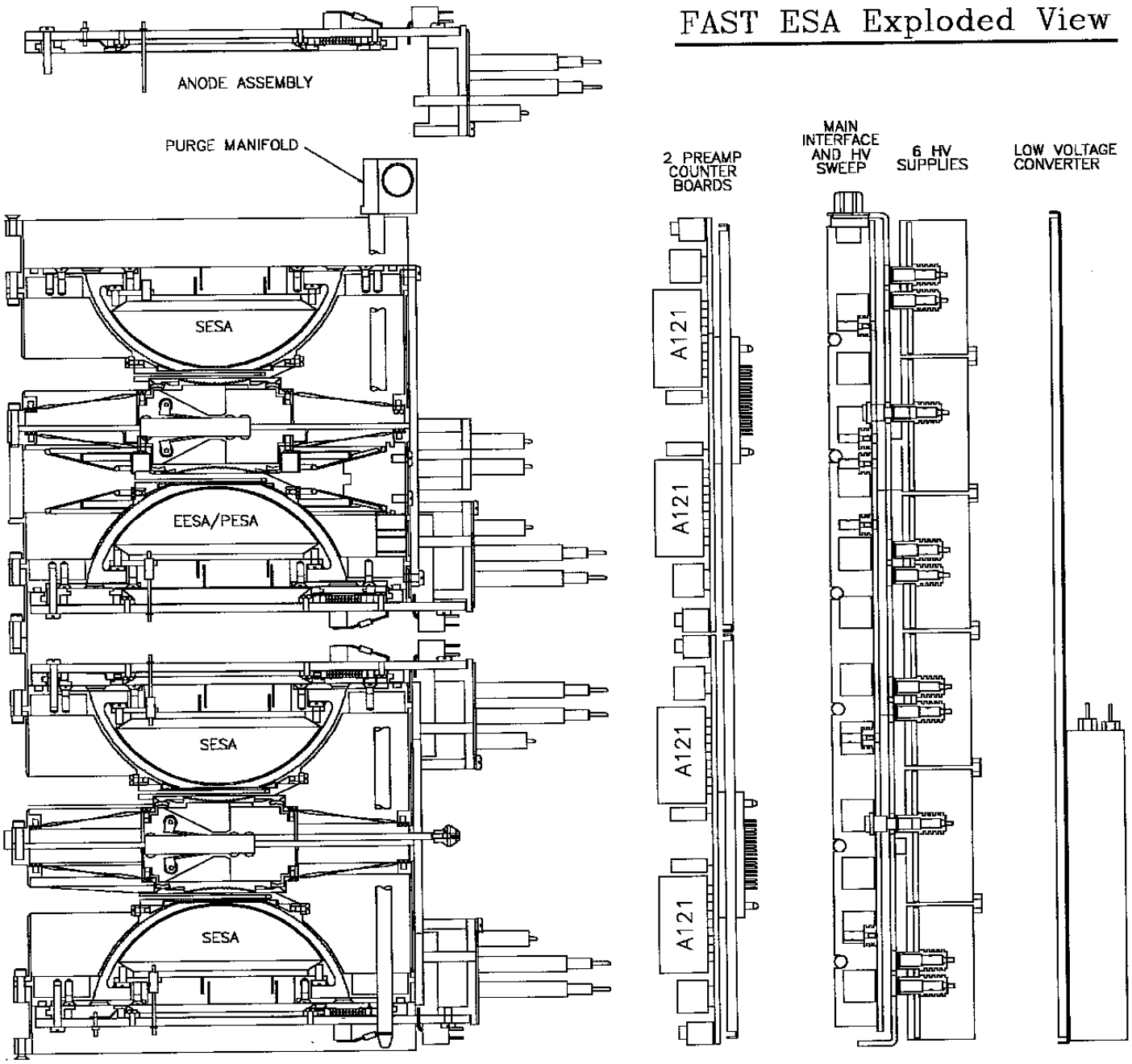

Fig. 13. An exploded view of one of four stacks of plasma analyzers from the FAST spacecraft. The modular design allows for convenient testing and calibration of individual analyzer and electronic subsystems. The modules plug directly together with no cable harnesses.

spoked retractor spring. Two analyzers share a common top cover plate, which also includes a sliding top hat closer mechanism.

The anode assembly includes the MCP mounting, HV circuitry and connectors, and the anode signal components. The cross section view (fig. 14) illustrates the MCP mounting and the multilayer circuit configuration. The MCP is clamped along its full periphery with etched Be-Cu spring mounts. This clamping assures that the plates make intimate contact and also provides a good thermal path from the plates. The signal path goes from the individual anode pads to a bleeder resistor and back to a HV coupling capacitor. The signal continues through a limit resistor to clamp diodes that protect the preamplifier from damage arising from any discharges in the anode high voltage circuit. The anode signal is finally routed through a connector to the preamp PC board. The high voltage is supplied to the anode by a direct path from the high voltage boards. The top of fig. 13 shows the long insulated pins protruding from the anode assemblies that make the high voltage connection.

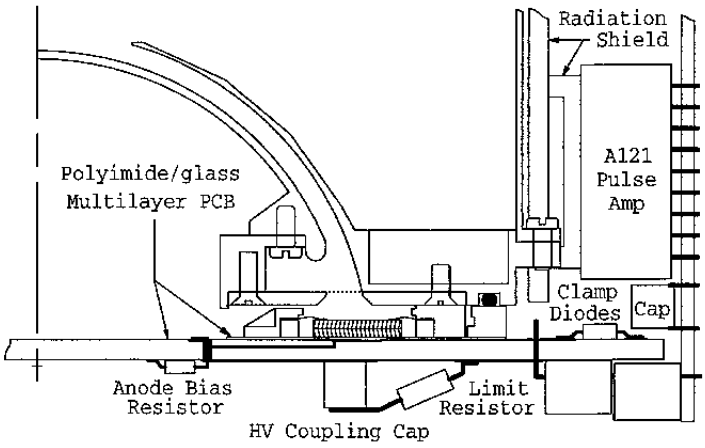

Fig. 14. A detail view of the MCP/anode board and preamplifier board interface for the FAST plasma analyzers. The MCPs are mounted on the anode board and completely tested and qualified as a subsystem before being installed in the analyzer assembly.

A final feature of the analyzer module is a purge manifold that feeds dry nitrogen purge gas to each of the anodes. The anode assembly includes a filter, meter orifice, and gas routing channel that distributes the purge gas to the MCP and analyzer's interior volume. The leaf spring on the top hat closer serves as a relief valve that maintains positive pressure within the analyzer. A small O-ring gland on each anode makes the sealed joint to the purge manifold "skewer" tube. The spacecraft is plumbed with a gas supply to each instrument that supplies purge during ground operations and storage.

The preamplifier boards are electrically and mechanically attached to the analyzer assembly to ensure good electrical grounding and noise isolation. The preamplifiers are Amptek A121 hybrid amplifier/discriminators that can operate at rates up to about 6 MHz. They have voltage programmable gain and resistor adjusted pulse width and dead time. Each amplifier board services two analyzers, with 8 channels for each SESA and 16 channels for the E/IESA spectrometers. The digital counter circuits are made from Actel field programmable gate arrays (FPGA). Eight separate 14 bit counters and readout circuitry are programmed into each FPGA. Other miscellaneous functions included in the FPGA include a test pulse generator with programmable amplitude. The D to A converter (DAC) to set the pulse amplitude is made by using a resistor network driven by the FPGA output drivers. The same test pulse is distributed to all amplifiers, and is simply coupled capacitively by appropriate overlay of PC board traces. No other discrete circuitry is needed for the amplifier boards.

The main interface board contains most of the control circuitry for the instrument. Virtually all logic circuitry for the instrument is imbedded in nine FPGAs. One of the FPGA circuits is the interface to the main Instrument Data Processor Unit (IDPU), and performs the command decoding and data routing functions. The remaining circuits on the interface board control high voltage operations. Although these gate array circuits are inherently digital, they also make excellent 16 bit DACs with the addition of simple resistor ladder networks, and a regulated power supply. The sweep generator circuits compute a variety of programmable waveforms and generate the DAC voltage outputs with a single active device. The fixed HV supplies are controlled by similar FPGA/DAC controllers. The sweep control voltages drive a set of optocoupled HV amplifiers to produce the fast high voltage waveforms. The settling time for a full scale 3 kV voltage step is about 2 ms.

A conspicuous departure from most current instruments is the lack of a microprocessor. In fact, the entire FAST science payload is controlled through a central science Instrument Data Processor (IDPU) system that has only a single microprocessor. Its main function is managing the mass memory, generating telemetry packet headers, and managing instrument health and general operations. The IDPU communicates with the instruments over a clocked serial interface, which also furnishes the measurement time base. The particle time base is the spin sector clock, running at 12,288 pulses per spin. One command or data transfer block can be executed at each sector pulse, and the data transfer rate is 131 KHz. The instrument has a number of "firmware" menus that can be selected for generating High Voltage sweep patterns. The counter data readout is completely controlled by the IDPU using data request commands.

A deliberate choice was made early in the project definition to use programmable logic for all "firmware" designs, and restrict software to only those functions that require on-orbit programmability. The FPGA technology has revolutionized instrument design at least as much as microprocessors. Each FPGA replaces from 20 to 50 discrete ICs, and allows very efficient digital design. Circuit boards can be designed and fabricated in parallel with logic development because package pin assignments are flexible. A final benefit of using firmware designs is to eliminate the delusion that designs can be "finished" in software after launch.

Acknowledgments. This work was supported by University of Washington grant UW/376990 and NASA grants NAG5-959, NGL-05-033-017, NAS5-30366, and NAS5-31283.

REFERENCES

Acuna, M., et al., Mars Observer magnetic fields investigation, *J. Geophys. Res.* 97, 7799, 1992.

Alsop, C., S. Scott, and L. Free, UV rejection design and performance of the PEACE electrostatic analyzers, this volume.

Bame, S.J., et al., *IEEE Trans. Geosci. Electr.* **GE-16**, 216, 1978.

Boehm, M.H., et al., The TESP electron spectrometer and correlator (F7) on Freja, *Space Sci. Rev.* **70**, 509, 1994.

Carlson, C.W., D.W. Curtis, G. Paschmann, and W. Michael, *Adv. Space. Res.*, **2**, 67, 1983.

Frank, L.A., D.M. Yeager, H.D. Ownes, K. L. Ackerson, and M. R. English, *IEEE Trans. Geosci. Electron.* **GE-16**, 221, 1978.

Gosling, J.T., J.R. Asbridge, S.J. Bame, and W.C. Feldman, *Rev. Sci. Instrum.* **49**, 1260, 1978.

Johnstone, A.D., et al., PEACE: a plasma electron and current experiment, in *Cluster: mission, payload and supporting activities*, ESA **SP-1159**, p. 163, 1993.

Lin, R.P., et al., A three-dimensional plasma and energetic particle investigation for the Wind spacecraft, *Space Sci. Rev.* **71**, 125, 1995.

McCarthy, M., and J.P. McFadden, Measurements of 0-25 eV ions with a retarding potential analyzer on the cluster ion spectroscopy experiment, this volume.

McFadden, J.P., and C.W. Carlson, Computer simulation in designing electrostatic optics for space plasma experiments, this volume.

McFadden, J.P., C. W. Carlson, and M.H. Boehm, Field-aligned electron precipitation at the edge of an arc, *J. Geophys. Res.* **91**, 1723, 1986.

Moebius, E., et al., The 3-D plasma distribution function analyzers with timeof-flight mass discrimination for CLUSTER, FAST, and Equator-S, this volume.

Paschmann, G., et al., *IEEE Trans. Geosci. Remote Sensing* **GE-23**, 262, 1983.

Sablik, M.J., D. Golimowski, J.R. Sharber, and J.D. Winningham, Computer simulation of a 360° field-of-view "top hat" electrostatic analyzer, *Rev. Sci. Instrum.* **59(1)**, 146, 1988.

Shelley, E.G., et al., *IEEE Trans. Geosci. Remote Sensing*, **GE-23**, 241, 1995.

Siegmund, O.H.W., and J. Stock, Performance of low resistance microchannel plate stacks, *EUV, X-Ray and Gamma-Ray Instrum. Astron., SPIE* **1549**, p. 81, 1991.

Siegmund, O.H.W., M.A. Gummin, J. Stock, and D. Marsh, Microchannel plate imaging detectors for the ultraviolet, Proc. ESA Symp. Photon Detectors Space Instrum., Noordwijk, Netherlands, 10-12 November 1992, SP-**356**, p. 89, 1992.

Walton, D.M., A.M. James, J.A. Bowles, A.D. Johnstone, High-speed 2-D imaging for plasma analyzers, this volume.

Young, D.T., et al., 2-π radian field-of-view toroidal electrostatic analyzer, *Rev. Sci. Instrum.* **59(5)**, 743, 1988.